communications biology

Article

https://doi.org/10.1038/s42003-024-06905-z

Structure of endothelin ET_B receptor–G_i complex in a conformation stabilized by unique NPxxL motif

Kazutoshi Tani[1,2,11,12] ✉, Saori Maki-Yonekura[3,11], Ryo Kanno[4,5], Tatsuki Negami[6], Tasuku Hamaguchi[3,7], Malgorzata Hall[4], Akira Mizoguchi[2], Bruno M. Humbel[8,9], Tohru Terada[6], Koji Yonekura[3,7] & Tomoko Doi[10,12] ✉

Endothelin type B receptor (ET_BR) plays a crucial role in regulating blood pressure and humoral homeostasis, making it an important therapeutic target for related diseases. ET_BR activation by the endogenous peptide hormones endothelin (ET)−1–3 stimulates several signaling pathways, including G_s, $G_{i/o}$, $G_{q/11}$, $G_{12/13}$, and β-arrestin. Although the conserved NPxxY motif in transmembrane helix 7 (TM7) is important during GPCR activation, ET_BR possesses the lesser known NPxxL motif. In this study, we present the cryo-EM structure of the ET_BR–G_i complex, complemented by MD simulations and functional studies. These investigations reveal an unusual movement of TM7 to the intracellular side during ET_BR activation and the essential roles of the diverse NPxxL motif in stabilizing the active conformation of ET_BR and organizing the assembly of the binding pocket for the α5 helix of G_i protein. These findings enhance our understanding of the interactions between GPCRs and G proteins, thereby advancing the development of therapeutic strategies.

The endothelin (ET) family comprises three endogenous isoforms (ET-1–3), each of which contains 21 amino acid residues and two intramolecular disulfide bonds. ET-1, the primary isoform in the human cardiovascular system, is one of the most abundant, potent, and long-lasting constrictors of blood vessels. ET-1 plays a significant role in physiological processes, such as modulation of basal vascular tone, regulation of sodium balance, development of neural crest cells, and cell proliferation, and development of pathophysiological conditions, such as cardiovascular disease, neurological disorders, renal disease, and cancer[1–5]. The ET family exerts its effects through ET receptors, specifically subtypes ET_A and ET_B (ET_AR and ET_BR, respectively), which belong to the β-subfamily of class-A G-protein-coupled receptors (GPCRs). The ET-bound receptors transmit signals through heterotrimeric G proteins with promiscuous coupling properties and also interact with β-arrestins[2,6–8].

GPCRs mediate cellular responses to various extracellular molecules, including lipids, nucleosides, neurotransmitters, hormones, and proteins. Ligand binding triggers structural changes in GPCRs, initiating signal transmission. Agonist-mediated GPCR activation is well understood, with specific conserved sequence regions, including $C^{6.47}W^{6.48}xP^{6.50}$, $P^{5.50}I^{3.40}F^{6.44}$, $N^{7.49}P^{7.50}xxY^{7.53}$, and $D^{3.49}R^{3.50}Y^{3.51}$ motifs (using Ballesteros–Weinstein numbering[9] for class-A GPCRs), playing successive roles[10–16]. Furthermore, three highly conserved residues: $R^{3.50}$ in DRY, $Y^{5.58}$, and $Y^{7.53}$ in NPxxY, play key roles in activating class-A GPCRs[11–15]. $Y^{7.53}$ in NPxxY acts as a switch for water rearrangement, in addition to the inward movement of the cytoplasmic end of TM7 during activation[17]. During this process, $N^{7.49}$ from NPxxY interacts directly with the conserved $D^{2.50}$ and $Y^{7.53}$ interacts with the highly conserved $Y^{5.58}$ in TM5, either directly or through a bridging water molecule known as the "water lock" in the active state[18,19]. Because $Y^{5.58}$ in

[1]Center for Computational Sciences, University of Tsukuba, 1-1-1 Tennodai, Tsukuba, Ibaraki, 305-8577, Japan. [2]Graduate School of Medicine, Mie University, 2–174 Edobashi Tsu, Mie, 514-8507, Japan. [3]RIKEN SPring-8 Center, 1-1-1, Kouto, Sayo, Hyogo, 679-5148, Japan. [4]Scientific Imaging Section, Research Support Division, Okinawa Institute of Science and Technology Graduate University (OIST), 1919-1, Tancha, Onna-son, Kunigami-gun, Okinawa, 904-0495, Japan. [5]Quantum Wave Microscopy Unit, Okinawa Institute of Science and Technology Graduate University (OIST), 1919-1, Tancha, Onna-son, Kunigami-gun, Okinawa, 904-0495, Japan. [6]Department of Biotechnology, Graduate School of Agricultural and Life Sciences, University of Tokyo, Bunkyo-ku, Tokyo, 113-8657, Japan. [7]Institute of Multidisciplinary Research for Advanced Materials, Tohoku University, 2-1-1 Katahira, Aoba-ku, Sendai, 980-8577, Japan. [8]Provost Office, Okinawa Institute of Science and Technology Graduate University (OIST), 1919-1, Tancha, Onna-son, Kunigami-gun, Okinawa, 904-0495, Japan. [9]Department of Cell Biology and Neuroscience, Juntendo University, Graduate School of Medicine, Tokyo, 113-8421, Japan. [10]Graduate School of Science, Kyoto University, Kitashirakawa Oiwake-cho, Sakyo-ku, Kyoto, 606-8502, Japan. [11]These authors contributed equally: Kazutoshi Tani, Saori Maki-Yonekura. [12]These authors jointly supervised this work: Kazutoshi Tani, Tomoko Doi. ✉e-mail: ktani@ccs.tsukuba.ac.jp; doi.tomoko.8n@kyoto-u.jp

TM5 undergoes rotation during activation and then stabilizes the orientation of $R^{3.50}$ through a hydrogen bond, $Y^{7.53}$ in NPxxY indirectly stabilizes the orientation of $R^{3.50}$ in DRY. Thus, $R^{3.50}$, $Y^{5.58}$, and $Y^{7.53}$ change their interactions during activation and structurally cooperate to generate the active state of class-A GPCRs. However, some class-A GPCRs have unique motifs such as the NPxxL found in ET_BR; how these conserved or divergent motifs contribute to the formation of binding pockets for heterotrimeric G proteins is unclear.

We determined the crystal structures of thermostabilized ET_BR in three forms: ET-1-bound, ligand-free, and antagonist bosentan-bound[20–22]. Although the ET-1-bound ET_BR structure detailed the binding of ET-1 to the receptor, it did not explain the activation mechanism, because the intracellular side was fixed in an inactive state by the insertion of T4 lysozyme into ICL3. To better understand ET_BR activation by ET-1 and its coupling with G proteins, we report the structure of the ET-1-bound ET_BR–G_i complex, determined using cryo-electron microscopy (cryo-EM), and further evaluated with MD simulations and mutagenesis studies. We identified a unique feature—the downward motion of TM7 during activation through a diverse NPxxL motif. This motion stabilized the active conformation of ET_BR, leading to the formation of a hydrophobic binding pocket for the C-terminal α5 helix of $G\alpha_i$.

Results

Overall structure of the ET-1-bound ET_BR–G_i complex

To facilitate complex formation, ET_BR and G_{i1} heterotrimer were expressed separately in Sf9 insect cells and combined after purification in lauryl maltose-neopentyl glycol (LMNG) and cholesteryl hemisuccinate (CHS). ET_BR was stabilized by introducing the $R124Y^{1.55}$ thermostabilizing mutation, which does not reduce ET-1 binding affinity and G-protein coupling ability[21]. Stabilization of the ET_BR–G_i complex was achieved by introducing four dominant negative mutations into the $G\alpha_{i1}$ subunit[23]. In addition, scFv16[24] was used to stabilize interactions between the α_{i1} and β subunits (Supplementary Figs. 1, 2). First, the structure of the ET-1-bound ET_BR–wild-type G_{i1}–scFv16 complex was analyzed by single particle cryo-EM at a global resolution of 4.6 Å (Table 1, Supplementary Figs. 1, 3). To improve resolution, the structure of the complex, including the dominant negative $G\alpha_{i1}$ subunit ($DNG\alpha_{i1}$), was determined with a global resolution of 3.2 Å (Fig. 1, Table 1, Supplementary Figs. 2, 4). Furthermore, we performed focused 3D refinement to obtain receptor densities at a resolution of 3.6 Å. Receptor density was assessed in the ET_BR–DNG_{i1} complex after adjusting the alignment center to the receptor (Table 1, Supplementary Figs. 2, 5). Both ET_BR–G_i complex models are nearly identical—their Cα atoms have an RMSD of 0.662 Å (Supplementary Fig. 6a). Compared with the ET-1 bound ET_BR model in ET_BR–DNG_{i1}, the small RMSD values of the Cα atoms and the similar residue conformations in the other two models indicate they are nearly identical (0.391 Å for ET_BR–wild-type G_{i1} and 0.364 Å for the focused 3D refinement of ET_BR) (Supplementary Fig. 6b, c). The G_{i1}-bound ET_BR structure displayed a typical outward movement of the cytoplasmic side of TM6 to a moderate extent (approximately 7 Å), similar to other class-A G_i-bound GPCRs (Supplementary Fig. 7). We used the ET-1-bound ET_BR–DNG_{i1}–scFv16 complex as the ET_BR–G_{i1} complex and analyzed structural changes in detail.

Structure of G_i-stabilized active ET_BR

The mode of ET-1 binding in the ET_BR–G_i complex closely resembled that of the crystal structure of ET-1-bound ET_BR. $Y13^{ET\text{-}1}$ and $F14^{ET\text{-}1}$ in the helical region of ET-1 played a pivotal role in the compact assembly of the N-terminal tail and the extracellular side of TM7, initiating helical rearrangements of ET_BR (Fig. 2a). This assembly is essential for full G-protein activation[25]. The C-terminal region of ET-1 ($L17^{ET\text{-}1}$–$W21^{ET\text{-}1}$) fits into the transmembrane orthosteric pocket of the receptor, interacting with many hydrophobic ($I157^{2.60}$, $L277^{5.42}$, $L339^{6.51}$, etc.) and hydrophilic (including $K182^{3.33}$, $K273^{5.38}$, $R343^{6.55}$, $D368^{7.35}$, etc.) residues[20]. The C-terminal side chain of $W21^{ET\text{-}1}$ directly interacted with $W336^{6.48}$ in the CWxP motif (Fig. 2b). Interactions between ET-1 and ET_BR, both in the transmembrane region surrounding the C-terminal region of ET-1 and close to the extracellular side, played a role in ET_BR activation. These ligand–receptor interactions influenced the helical rearrangement of ET_BR through the conserved $V189^{3.40}P285^{5.50}F332^{6.44}$ motif, resulting in an inward rotation of $R199^{3.50}$ and $Y293^{5.58}$, an outward movement of the cytoplasmic side of TM6 (Fig. 2b, c), and crevice formation on the cytoplasmic side of the receptor to accommodate $G\alpha_i$.

As observed in other class-A GPCRs, the outward shift of TM6 disrupted the salt bridge between $D198^{3.49}$ and $R199^{3.50}$ of DRY, seen in the ET-1-bound inactive ET_BR. $R199^{3.50}$ extended toward TM7, stabilized by $Y293^{5.58}$ through hydrogen bonding (Fig. 2d, Supplementary Fig. 8a). A simultaneous downward displacement (~ 1.5 Å) at the NPxxL motif ($N382^{7.49}$, $P383^{7.50}$, and $L386^{7.53}$ in ET_BR instead of $Y^{7.53}$) was observed in the ET-1–ET_BR–G_i complex (Fig. 2e). $N382^{7.49}$ extended toward $R199^{3.50}$, and $L386^{7.53}$ formed a hydrophobic interaction with $I140^{2.43}$ to stabilize the helical contacts between TM2 and TM7 (Figs. 2e and 3a). Because the residue at $386^{7.53}$ was leucine, and not the conserved tyrosine, the hallmark water-mediated hydrogen bonding network, including $Y^{7.53}$ and $R^{3.50}$, which is characteristic of class-A GPCR activation (Supplementary Fig. 8b), was not formed.

Structural comparisons across class-A GPCRs indicated a conserved rearrangement of residue contacts at positions 3.46 and 7.53 upon activation[10]. In many class-A GPCRs with the conserved $Y^{7.53}$ sequence in the active state, distances between residues 3.46 and 7.53 are typically ≤4.5 Å, allowing for hydrophobic or van der Waals interactions. However, for ET_BR, the distance between $L195^{3.46}$ and $L386^{7.53}$ was approximately 7.3 Å without direct contact, because the absence of $Y^{7.53}$ and downward shift of TM7 created a space between them (Fig. 3a). The side chains of the rotated $R199^{3.50}$ and $N382^{7.49}$ extended toward this space, where possible water molecules were detected (Fig. 3a, Supplementary Fig. 8a). In a later section, we validated the presence of water molecules using MD simulations.

The downward shift of TM7 was stabilized by a hydrophobic interaction between $L386^{7.53}$ and $I140^{2.43}$, which simultaneously interacted with $L195^{3.46}$ (Fig. 3a). Despite the considerable distances between residues 3.46 and 7.53, precluding direct contacts, this conformation could be maintained. Furthermore, $V389^{7.56}$, located one turn downward from $L386^{7.53}$ in TM7 of ET_BR, contacted $T324^{6.36}$ in TM6, as seen in other class-A GPCRs with the conserved $Y^{7.53}$ (Fig. 3b). Remarkably, residues $S390^{8.47}$ and $V325^{6.37}$, which are adjacent and play crucial roles as binding sites for the α5 helix of $G\alpha_i$ (described in the next section), were appropriately arranged in the active conformation of ET_BR through the downward motion of TM7. Hence, although the unique $382N^{7.49}Pxx386L^{7.53}$ motif creates an unusual space between $L195^{3.46}$, $R199^{3.50}$, $N382^{7.49}$, and $L386^{7.53}$ (Fig. 3a, Supplementary Fig. 8a), a binding pocket for the α5 helix of $G\alpha_i$ was established in the active structure of ET_BR (described ahead). This unusual space can be observed in the area between $V126^{3.46}$ and $Y305^{7.53}$ of NK_1R, comprising the NPxxY motif[26,27]. The surrounding area demonstrates an active conformation like ET_BR, characterized by a downward shift of the cytoplasmic end of TM7, contrasting with the other GPCRs with the NPxxY motif (Fig. 3c, Supplementary Fig. 8; see the Discussion section).

The biological importance of these interactions in the active conformation of ET_BR was confirmed through the dissociation of heterotrimeric G proteins associated with its activation[7,28] (Fig. 2f, g, Supplementary Fig. 9, Table 1). Mutations $R199^{3.50}A$, $Y293^{5.58}F$, and $N382^{7.49}A$, resulted in nearly complete impairment in the G_i-protein dissociation assay. Additionally, although hydrophobic mutations of $L386^{7.53}$ to Ile and Val reduced dissociation activities by approximately 50% when considering their expression levels (Supplementary Table 1), mutations of $L386^{7.53}$ to hydrophilic or small residues, such as Tyr, Ala, or Asn, resulted in severely impaired activities. The importance of these residues in forming the active conformation was confirmed through the GloSensor cAMP accumulation assay (Promega) through G_s coupling. We observed severe impairment due to mutations, which is consistent with the findings of the G_i dissociation assay (Supplementary Fig. 10a, b, Supplementary Table 2). Thus, interactions between $R199^{3.50}$, $Y293^{5.58}$, and $N382^{7.49}$ are biologically essential for G_i-protein activation, and the bulky hydrophobic residue leucine at $386^{7.53}$ is important for the active conformation of ET_BR.

Table 1 | Cryo-EM data collection, refinement and validation statistics of the ET_B receptor-G_i complexes

	ET-1 bound ET_BR-DNG_i-scFv16 (EMDB-38740, PDB-8XWP)		ET-1 bound ET_BR-DNG_i-scFv16 (focused ET_BR) (EMDB-60404, PDB-8ZRT)	ET-1 bound ET_BR-wild type G_i-scFv16 (EMDB-38741, PDB-8XWQ)
Data collection and processing				
Microscope	JEOL CRYO-ARM300			TF Talos Arctica
Camera	K3			Falcon III
Magnification	60,000	100,000		92,000
Voltage (kV)	300	300		200
Electron exposure (e–/Å^2)	53.3	49.2		40
Defocus range (μm)	–0.5 to –2.7	–0.6 to –3.5		–0.7 to –2.9
Calibrated pixel size (Å)	0.816	0.507		1.094
Detector physical pixel size (μm)	5			14
Symmetry imposed	C1			C1
Initial particle images (no.)	1,193,302	1,757,339	1,038,215	954,972
Final particle images (no.)	556,576	481,639	401,671	278,209
Map resolution (Å)	3.2		3.6	4.6
FSC threshold	0.143		0.143	0.143
Map resolution range (Å)	5.4–3.1		8.7–3.6	6.9–4.4
Refinement				
Initial model used (PDB code)	5GLH, 6OS9		8XWP	5GLH, 6OS9
Model resolution (Å)	3.2		4.1	4.6
FSC threshold	0.5		0.5	0.5
Model resolution range (Å)	120–3.2		120–3.6	126–4.6
Map sharpening *B* factor (Å^2)	–100		-100	–263
Model composition				
Non-hydrogen atoms	9076		2322	9076
Protein residues	1163		303	1163
B factors (Å^2)				
Protein	80.7		48.9	191.8
R.m.s. deviations				
Bond lengths (Å)	0.002		0.003	0.003
Bond angles (°)	0.473		0.693	0.546
Validation				
MolProbity score	2.31		1.82	2.59
Clashscore	8.97		13.56	14.24
Poor rotamers (%)	5.56		0.81	7.98
Ramachandran plot				
Favored (%)	96.06		96.93	96.33
Allowed (%)	3.94		3.07	3.67
Disallowed (%)	0.00		0.00	0.00

ET_BR–G_i interface

The structure of the ET_BR–G_i complex (Fig. 1a, Supplementary Fig. 7) revealed a mode of interaction similar to that in other G_i-bound receptors. However, the interactions between ET_BR and G_i were exclusively mediated through the α5 helix of $G\alpha_i$. This helix binds ET_BR in a more vertical orientation in ET_BR–G_i than in other GPCR–G_s or G_q structures (Supplementary Fig. 7). Consequently, the C-terminus of the α5 helix of $G\alpha_i$ dominantly bound ET_BR, which confined the ET_BR–G_i interface within a relatively narrow area.

A significant interface between ET_BR and $G\alpha_{i1}$ was formed by TM3, TM5, TM6, TM7, ICL1, and ICL2 of the receptor, in addition to the last 15 residues of the C-terminal α5 helix (residues 340–351) and the following three-residue wavy hook (352-GLF-354) of $G\alpha_i$ (Fig. 4a). In detail, as observed in many G_i-bound GPCR complexes, the apex of the α5-helix engaged with the end of TM7 and helix 8. At this interface, the backbone carbonyl of $G353^{H5.24}$ (superscripts refer to the CGN numbering system)[29] and C-terminal carboxylate of $F354^{H5.26}$ formed hydrogen bonds with the side chain of $S390^{8.47}$ and the backbone carbonyl of $V389^{7.56}$ of ET_BR. $G\alpha_i$ residues, including $D341^{H5.13}$, $N347^{H5.19}$, and $D350^{H5.22}$, established four hydrogen bonds with ET_BR residues $N134A^{ICL1}$, $R208^{ICL2}$, $K210^{ICL2}$, and $R318^{6.30}$ (Supplementary Table 3).

However, the amino acid residues located between the cytoplasmic cleft of ET_BR and the α5 helix of $G\alpha_i$ predominantly formed van der Waals interactions for the pairs $C351^{H5.23}$–$R199^{3.50}$ and $N347^{H5.19}$–$A202^{3.53}$ (Fig. 4, Supplementary Table 3). Notably, the large side chains of $L348^{H5.20}$ and $L353^{H5.25}$ nestled deeply into the hydrophobic pocket formed by $V203^{3.54}$, $M296^{5.61}$, $M300^{5.65}$, $V321^{6.33}$, $V325^{6.37}$, and

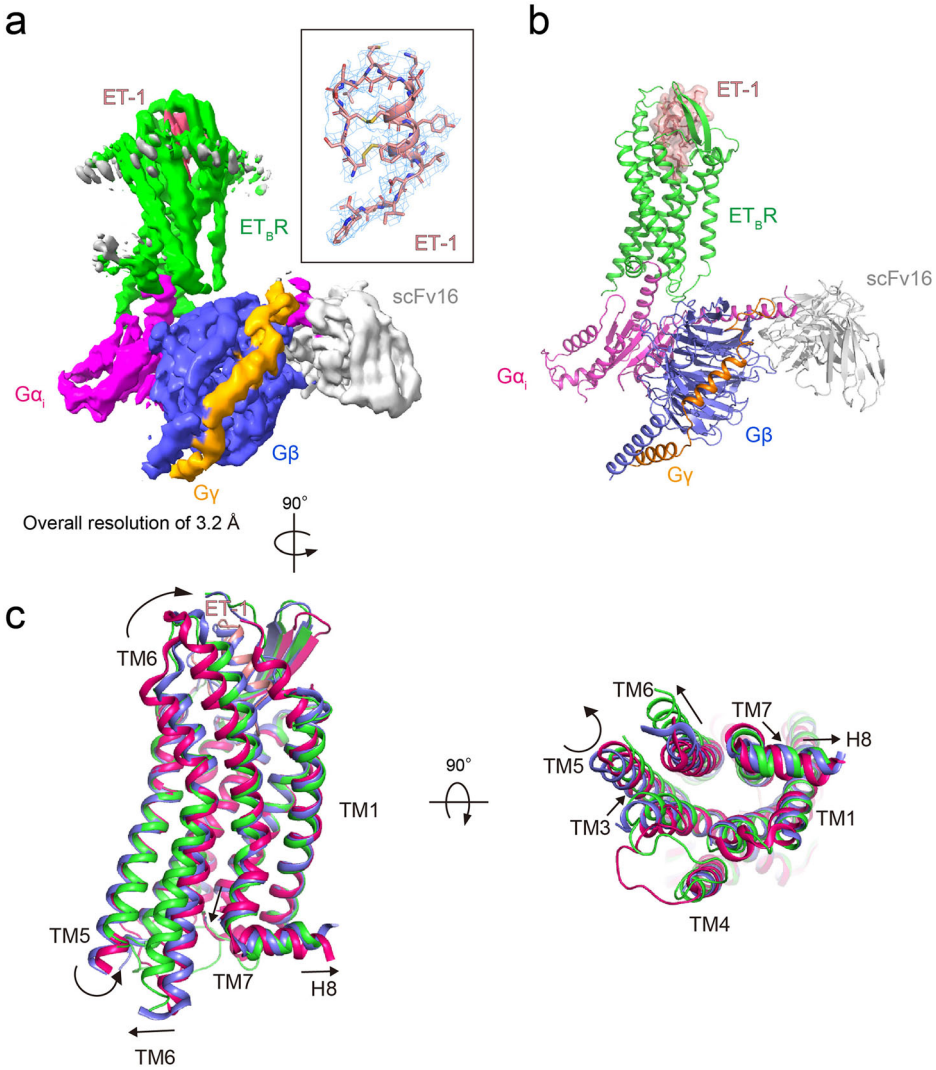

Fig. 1 | Cryo-EM structure of the ET-1–ET$_B$R–DNG$_i$ complex. a Cryo-EM density map of the ET-1–ET$_B$R–DNG$_i$–scFv16 complex. Green: ET$_B$R, salmon: ET-1, magenta: DNGα$_i$ Ras-like domain, blue: Gβ, orange: Gγ, and gray: scFv16. The inset shows the ET-1 model with the corresponding density at a contour level of 4.0 σ. **b** Molecular model of the ET-1–ET$_B$R–DNG$_i$ complex in the same view and color scheme as in **a**. **c** Comparison of the G$_i$-stabilized active state of ET-1–ET$_B$R (green), partially active state of ET-1–ET$_B$R (blue), and bosentan-bound inactive ET$_B$R (red). Black arrows represent helical movements from inactive to active state of ET$_B$R.

V389$^{7.56}$ in TM3, TM5, TM6, and TM7 of ET$_B$R (Fig. 3b). The hydrophobic residues I344$^{H5.16}$ and I343$^{H5.15}$ formed interactions with W206^{ICL2} and I209^{ICL2}, respectively. Although residues at the C-terminal side of the α5 helix of Gα$_i$ interacted with residues within the ET$_B$R hydrophobic pocket, residues in the middle part of the α5 helix, such as T340$^{H5.12}$, D341 $^{H5.13}$, and I343 $^{H5.15}$, interacted with residues in ICL2, such as W206^{ICL2} and I209^{ICL2}, or close to ICL3, such as H314$^{6.26}$ and R318$^{6.30}$. Thus, the α5 helix of Gα$_i$ binding to ET$_B$R showed a relatively vertical orientation (Supplementary Fig. 7). This resulted in a shorter cytoplasmic side of TM5 compared with other class-A GPCRs, and the ICL2 of ET$_B$R formed a flexible loop.

ET$_B$R-G$_i$ dissociation assay

These structural observations were validated using an ET$_B$R-stimulated G$_i$-protein dissociation assay to examine the recognition determinants. The each ET$_B$R mutant receptor retained the affinity for ET-1 comparable to that of the wild-type (Supplementary Table 4). Among ET$_B$R mutations, S390$^{8.47}$A, M296$^{5.61}$A, M300$^{5.65}$A, and V325$^{6.37}$A substantially reduced the coupling between the receptor and Gα$_i$ by approximately 50%, whereas N134^{ICL1}A, H314$^{6.26}$A, R318$^{6.30}$A, V389$^{7.56}$A, and K391$^{8.48}$A mutations retained comparable or slightly reduced activities compared with wild-type, considering the expression of mutant receptors (Fig. 5a–c, Supplementary Table 1c–e). By contrast, among Gα$_i$ mutations, replacing L353$^{H5.25}$ with alanine severely impaired coupling with ET$_B$R, whereas G352A$^{H5.24}$ and K345A$^{H5.17}$ mutations decreased coupling by 50%. C351A$^{H5.23}$ and F354A$^{H5.26}$ mutations showed a slight reduction, whereas D341A$^{H5.13}$ and D350A$^{H5.22}$ mutations did not exhibit marked defects (Fig. 5d, Supplementary Table 1f). These findings are consistent with extensive mutagenesis studies of Gα$_{i1}$ on the stability and formation of the rhodopsin–G$_i$ complex, where L353A$^{H5.25}$, G352A$^{H5.24}$, and L348A$^{H5.20}$ substitutions severely impaired coupling, and C351A$^{H5.23}$, K345A$^{H5.17}$, and I344A$^{H5.16}$ substitutions reduced complex formation efficiencies to approximately 60%[30]. Therefore, coupling efficacies affected by mutations in ET$_B$R and the α5 helix of Gα$_i$ corresponded well with each other, reflecting their interactions at the observed interface of the complex. Notably, interactions at the end of TM7 and helix 8 of ET$_B$R with the C-terminus of the Gα$_i$ α5 helix, as well as the hydrophobic pocket composed of V203$^{3.54}$, M296$^{5.61}$, M300$^{5.65}$, and V325$^{6.37}$ with the C-terminal L348$^{H5.20}$ and L353$^{H5.25}$ of Gα$_i$ α5 helix, play crucial roles in ET$_B$R–G$_i$ coupling.

Most residues of the C-terminal α5 helix (T340–F354) interacted with ET$_B$R in the complex, except K345$^{H5.17}$, which interacted with F354$^{H5.26}$ through a cation–π interaction, and with D341$^{H5.13}$ and E318$^{h4s6.12}$ through salt bridges within Gα$_{i1}$ (Supplementary Fig. 11). In the GDP-bound form, K345$^{H5.17}$ did not interact with D341$^{H5.13}$ or E318$^{h4s6.12}$, which was originally located at the end of the β6 sheet. The translation and twist of the α5 helix during coupling with ET$_B$R led to K345$^{H5.17}$ interacting with D341$^{H5.13}$ and E318$^{h4s6.12}$. This interaction stabilized the twisted α5 helix and the conformation of the shortened β6 sheet as well as the GDP-released β6-α5 loop. The K345A$^{H5.17}$ mutation led to an approximately 50% reduction in the G$_i$ dissociation assay (Fig. 5d) and the rhodopsin–G$_i$ complex formation assay[30], indicating that K345$^{H5.17}$ plays a fundamental role in G$_i$ activation.

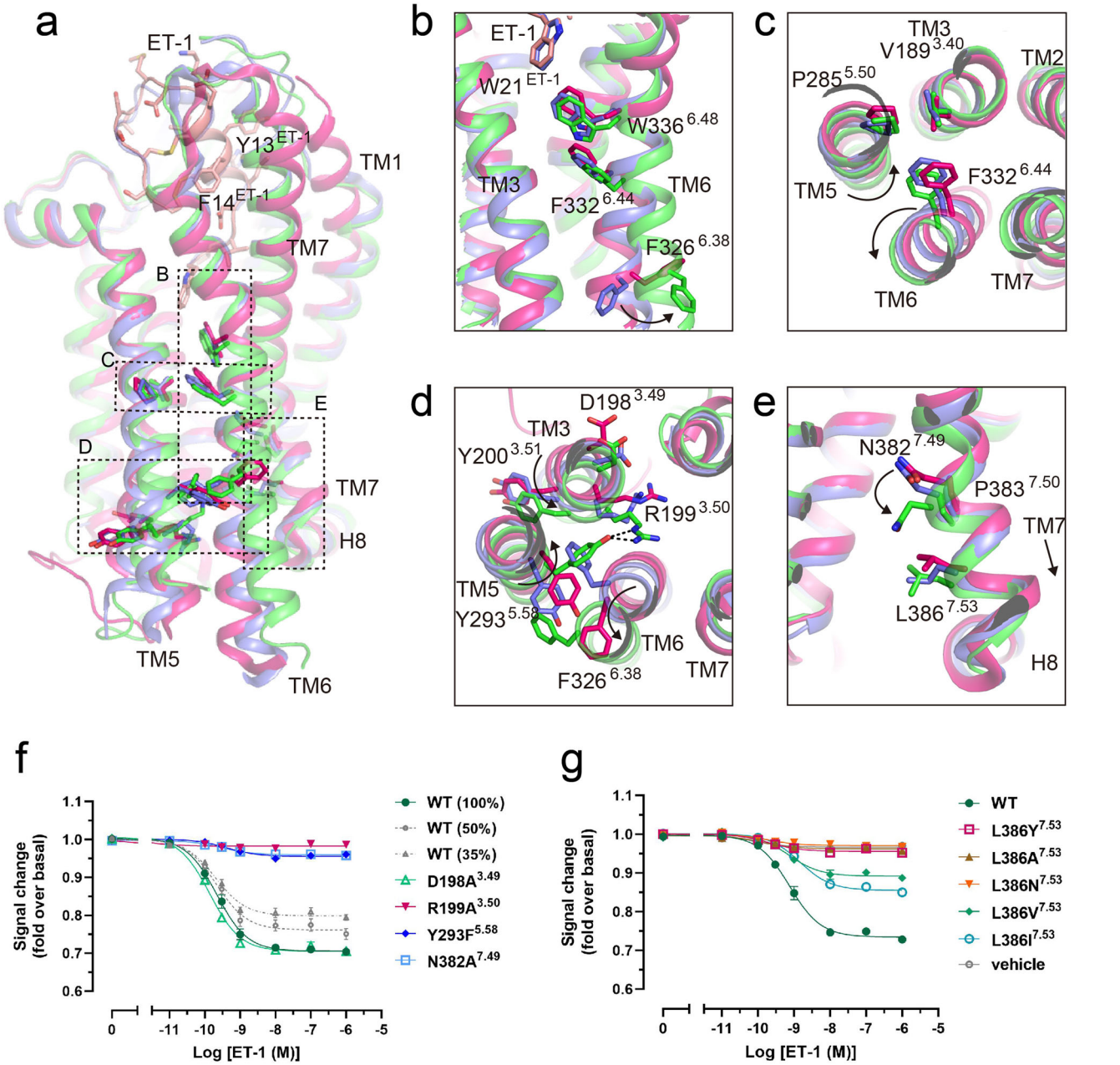

Fig. 2 | G_i-coupled ET_BR is in an active conformation. a Superposition of the G_i-bound ET_BR structure (green) with the partially active-state crystal structure of ET-1-bound ET_BR (blue) and the inactive-state crystal structure of the antagonist bosentan-bound ET_BR (magenta). **b**–**e** Close-up views of conserved motifs involved in receptor activation. Arrows indicate the repositioning of side chains from the inactive to active state. **f**, **g** Concentration–response curves for ET-1-induced G_i signaling activity in the NanoBiT G-protein dissociation assay of ET_BR–wild-type (WT) and mutant receptors. Symbols and error bars represent mean and standard error of the mean (SEM), respectively, from three independent experiments, each performed in duplicate or triplicate. Signaling of reduced amounts of WT ET_BR (% of plasmid DNA transfected) for G_i is shown in gray. Data for these figures and expression levels of WT and mutant receptors measured by [^{125}I]ET-1 binding are shown in Supplementary Fig. 8 and Table 1a, b.

This role includes modulating the location of C-terminal F354$^{H5.26}$ and stabilizing the ET_BR–G_i complex.

ET_BR coupled through the C-terminus of Gα

The α5 helix comprises conserved and variable residues across Gα proteins and could serve as a common mode of interaction with various types of GPCRs or as a selective mode of interaction based on receptor specificity[29]. The structural insights provided by the ET_BR–G_i structure, in addition to the results of biological validation, suggest that conserved hydrophobic residues, particularly L348$^{H5.20}$ and L353$^{H5.25}$, play pivotal roles in coupling (Figs. 4b and 5d). These residues form numerous contacts with specific residues in the hydrophobic binding pocket of ET_BR. When these residues are substituted with others, coupling is significantly impaired (Fig. 5b, Supplementary Fig. 10c). Additionally, subtype-specific residues involved in Gα selectivity, such as C351$^{H5.23}$ and G352$^{H5.24}$, occupied crucial positions in the complex and established contacts with the central residues of ET_BR, including R199$^{3.50}$ and L386$^{7.53}$ (Figs. 2f, g, 5a, d, Supplementary Fig. 10, Tables 1, 2). Notably, the primary interactions of ET_BR with the α5 helix of $Gα_i$ are limited to the transmembrane area. This is because the binding of the C-terminal α5 helix to ET_BR occurs in a relatively vertical orientation, and ICL2 of ET_BR is a flexible loop. Consequently, in the coupling of ET_BR with other subfamilies, such as G_s, G_q, and G_{12}, it is likely that the conserved

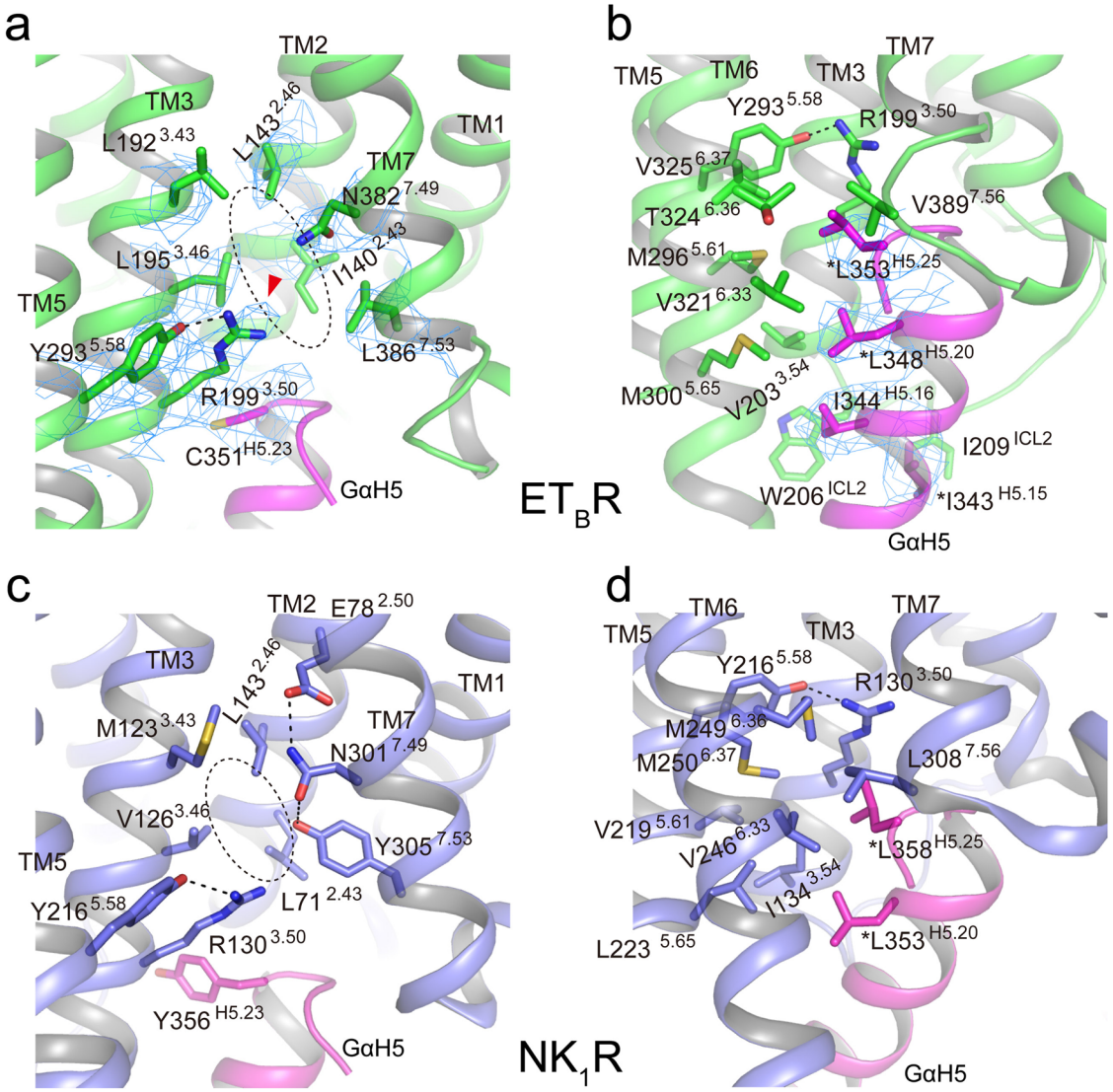

Fig. 3 | Hydrophobic interactions between ET_BR and NK_1R in the active state. Hydrophobic interactions around $R^{3.50}$ and $L/Y^{7.53}$ of ET_BR (**a**, **b**) and NK_1R (**c**, **d**), respectively. **a** The downward motion of TM7 of ET_BR is stabilized by $N382^{7.49}$ and $L386^{7.53}$ in the NPxxL motif through a series of hydrophobic interactions with $I140^{2.43}$, $L195^{3.46}$, etc. The density around all rendered residues at a contour level of 5.0 σ is shown as a mesh. **b** The large hydrophobic side chains of $L348^{H5.20}$ and $L353^{H5.25}$ of $G\alpha_i$ penetrate deeply into the hydrophobic pocket formed by TM3, TM5, TM6, and TM7 of ET_BR. $I343^{H5.15}$ and $I344^{H5.16}$ form additional interactions with ICL2. The density around the rendered residues of the α5 helix of $G\alpha_i$ is shown as a mesh at a contour level of 5.0 σ. **c** The downward motion of TM7 of NK_1R is stabilized by $E78^{2.50}$, $N301^{7.49}$, and $Y305^{7.53}$ in NPxxY through a series of hydrogen-bond interactions as well as hydrophobic interactions with $L71^{2.43}$, $V126^{3.46}$, etc. **d** The large hydrophobic side chains of $L353^{H5.20}$ and $L358^{H5.25}$ of $G\alpha_q$ penetrate deeply into the hydrophobic pocket formed by TM3, TM5, TM6, and TM7 of NK_1R. Identical residues among G_i, G_o, and G_s are denoted by "*" before the amino acid label, but a conserved residue ($L348^{H5.15}$ of $G\alpha_q$) in **d** was omitted because it does not contact the receptor. The NPxxL motif leads to the formation of a larger cavity than NPxxY (indicated by a dashed oval).

$L348^{H5.20}$ and $L353^{H5.25}$ continue to play central roles as binding partners through a common mode of interactions (Fig. 3b, d). ET_BR may further adapt to selectively accommodate subtype-specific residues, such as H5.23 and H5.24, based on the requirements of the G-protein subfamily[29]. These distinctive features would enable ET_BR to exhibit promiscuity in coupling with G-protein subfamilies[2,6,7].

ET_BR–G_i interactions in molecular dynamics simulations

We performed molecular dynamics (MD) simulations of the ET-1–ET_BR–G_i complex to evaluate the key interactions for ET_BR–G_i activation. The simulations, each lasting 500 ns, were repeated three times with different initial velocities. The time evolutions of the Cα RMSDs of ET_BR, $G\alpha_i$, Gβ, and Gγ from the initial structures are shown in Supplementary Fig. 12a. The structures of ET_BR, Gβ, and Gγ remained stable during MD simulations with consistent RMSD values of <3 Å. However, $G\alpha_i$ underwent substantial conformational changes due to the large flexibility of its activated form. The Cα RMSDs of ET-1 and the C-terminal α5 helix of $G\alpha_i$ (residues 335–354) were calculated after superposing the Cα atoms of ET_BR on those of the initial structure (Supplementary Fig. 12b). No significant change occurred in either run, indicating stable binding of ET-1 and $G\alpha_i$ to ET_BR. We calculated the probabilities of hydrogen-bond formation for pairs $D341^{H5.13}$–$R318^{6.30}$, $N347^{H5.19}$–$R208^{ICL2}$, $D350^{H5.22}$–$N134^{ICL1}$, and $F354^{H5.26}$–$S390^{8.47}$ to analyze the stability of intermolecular interactions (Fig. 6a, Supplementary Table 5). Hydrogen bonds for pairs $D341^{H5.13}$–$R318^{6.30}$ and $F354^{H5.26}$–$S390^{8.47}$ were stably formed with probabilities of approximately 0.7. Although the hydrogen bond between $D350^{H5.22}$ and $N134^{ICL1}$ was broken after 130 ns of run 3, it was formed in runs 1 and 2 with probabilities of approximately 0.7 and 0.4, respectively, indicating the formation of a weak bond. By contrast, $N347^{H5.19}$ and $R208^{ICL2}$ rarely formed a hydrogen bond, because $R208^{ICL2}$ exhibited high structural flexibility. Next, we analyzed intermolecular

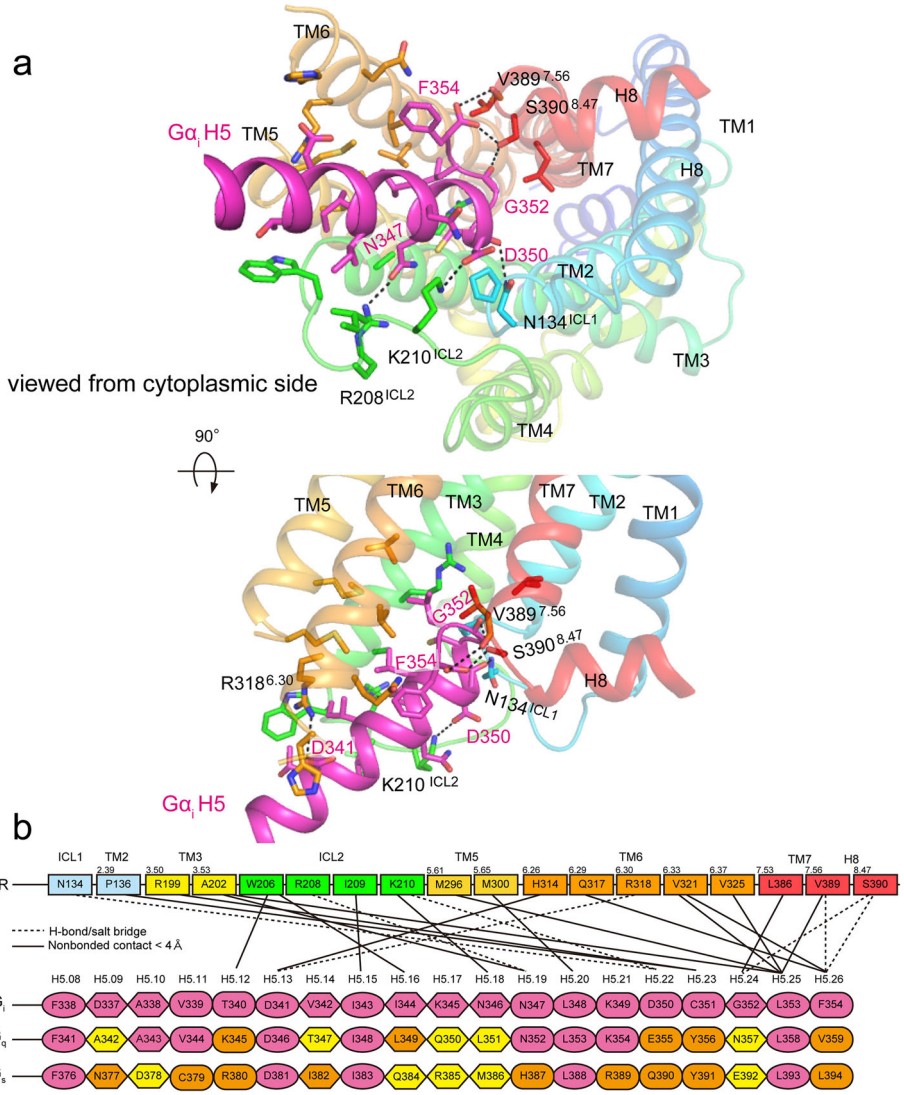

Fig. 4 | Interface between ET_BR and $G\alpha_i$. a Close-up view of the interaction between ET_BR and the α5 helix of $G\alpha_i$. Hydrogen bonds are indicated by black dotted lines. **b** Schematic representation of direct contacts between ET_BR and the α5 helix of $G\alpha_i$. Hydrogen-bonded and hydrophobic contacts are indicated by dashed and solid lines, respectively. Receptor residues involved in hydrogen bonding are numbered according to Ballesteros–Weinstein numbering[9], and $G\alpha_i$ residues involved in hydrogen bonding are numbered according to CGN numbering[29]. $G\alpha_i$ and conserved $G\alpha_q$ and $G\alpha_s$ residues are in magenta, homologous residues of $G\alpha_q$ and $G\alpha_s$ are in orange, and others are shown in yellow.

hydrogen bonds within ET_BR for pairs $D147^{2.50}$–$N382^{7.49}$, $D147^{2.50}$–$S379^{7.46}$, and $R199^{3.50}$–$Y293^{5.58}$. Hydrogen bond $D147^{2.50}$–$S379^{7.46}$ was stable in all runs. Hydrogen bonds for pairs $D147^{2.50}$–$N382^{7.49}$ and $R199^{3.50}$–$Y293^{5.58}$ were weak because they formed only in runs 1 and 2. Additionally, we calculated the average water occupancy in the intracellular cavity of ET_BR using the 500 ns trajectory of run 1 to analyze water-mediated interactions (Fig. 6b). Water densities exceeding 2-fold bulk density were observed in the cavity surrounded by $L195^{3.46}$, $R199^{3.50}$, $N382^{7.49}$, and $L386^{7.53}$. Minimum distances for the pairs $R199^{3.50}$–$N382^{7.49}$ and $L195^{3.46}$–$L386^{7.53}$ settled at approximately 7 and 6 Å, respectively (Fig. 6c, d). Thus, MD simulations revealed a water-mediated hydrogen-bond network connecting the area of $Y293^{5.58}$–$R199^{3.50}$–water molecules–$N382^{7.49}$–$S379^{7.46}$–$D147^{2.50}$ residing at the center of ET_BR. Accordingly, a relatively bulky density at the tip of $R199^{3.50}$ observed in the cryo-EM map can be attributed to water, contributing to the network (an arrowhead in Fig. 3a). This network was sealed by hydrophobic interactions through $L195^{3.46}$, $I140^{2.43}$, and $L386^{7.53}$, and ultimately completed by the binding of the α5 helix of $G\alpha_i$ to the receptor.

Discussion

The diversity in residue $L386^{7.53}$ within NPxxL in TM7 is crucial for the active conformation of ET_BR. Surprisingly, L386Y, as well as L386N/A, mutant receptors severely impaired G-protein activation (Fig. 2g, Supplementary Fig. 10b). Only the hydrophobic mutant receptor L386I/V retained approximately 50% of the activity. The mutant receptors indicate that a bulky hydrophobic residue at position 7.53 is indispensable for the active conformation of ET_BR. In the common rearrangement that occurs upon activation, direct contacts occur between residues at positions 7.53 and 3.46[10]. However, $L386^{7.53}$ was distant from $L195^{3.46}$ in ET_BR and linked with it through $I140^{2.43}$ through hydrophobic interactions, presumably to maintain hydrophilic interactions and form stable contacts in the active conformation of ET_BR (Fig. 3a). In addition, downward-shifted $L386^{7.53}$ positions $V389^{7.56}$ one turn below in TM7 adequately to create the binding site for $G\alpha_i$. Both $V389^{7.56}$ and the adjacent $S390^{8.47}$, located at the transition of TM7 to helix 8, interact with the C-terminal region of $G\alpha_i$, specifically the backbone carbonyl of $G352^{H5.24}$ and the C-terminal carboxylate of $F354^{H5.26}$ (Figs. 3b and 4a). These interactions play crucial roles in coupling (Fig. 5a, d, Supplementary Fig. 10). $V389^{7.56}$ interacts closely with $T324^{6.36}$ in TM6, adjacent to $V325^{6.37}$, which interacts with $M296^{5.61}$ in TM5, under which $M300^{5.65}$ is positioned one turn below, and which in turn is close to $V203^{3.54}$. Altogether, $V325^{6.37}$, $M296^{5.61}$, $M300^{5.65}$, and $V203^{3.54}$ align to form a hydrophobic core to bind the C-terminal $L353^{H5.25}$ and $L348^{H5.20}$ of α5 helix of $G\alpha_i$. These interactions constitute one of the primary binding determinants (Fig. 5b, d, Supplementary Fig. 10c). Coordinating with $V389^{7.56}$, the diverse $N^{7.49}PxxL^{7.53}$ motif plays a structural role in the active conformation of ET_BR through a downward shift, similar to NPxxY. In class-A GPCRs, approximately 4% of the receptors possess the $N^{7.49}P^{7.50}xxX^{7.53}$ sequence (X is leucine, phenylalanine, threonine, histidine, and so on (GPCRdb, http://www.gpcrdb.org) on the cytoplasmic side of TM7, such as ET_AR[31] and

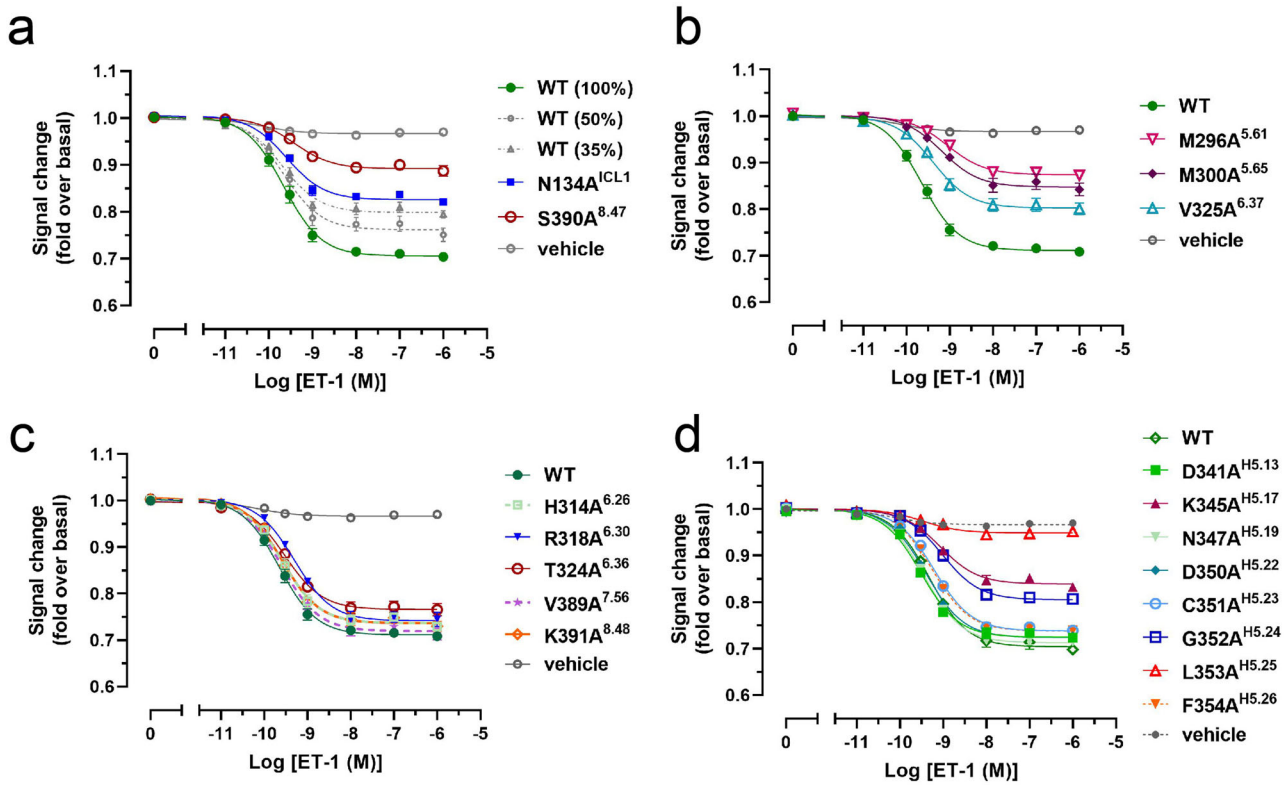

Fig. 5 | Validation of the interface residues of the ET_BR–G_i complex in the NanoBiT G_i-protein dissociation assay. Symbols and error bars represent mean and standard error of the mean (SEM), respectively, from three independent experiments, each performed in duplicate or triplicate. **a**–**c** The replaced interface residues of ET_BR were examined. Data for these figures and the expression levels of WT and mutant receptors are shown in Supplementary Table 1c–e. **d** The replaced interface residues of $G\alpha_i$ were examined. Mutant G_i show luminescence counts comparable with those of WT. Data for this figure are shown in Supplementary Table 1f.

GRPR/BB_2[32]. In these receptors, $L^{7.53}$ may contribute to the organization of a binding pocket for Gα, similar to that observed in ET_BR. Alternatively, NK_1R (with NPxxY) shows an unusual downward shift of the cytoplasmic end of TM7 upon activation. Because $N301^{7.49}$ of NK_1R forms direct hydrogen bonds with $E78^{2.50}$ and $Y305^{7.53}$ in the active state, and the cytoplasmic side of TM7 does not shift inward, but to the intracellular side upon activation, due to the longer side chain of $E78^{2.50}$ at position $D^{2.50}$ (Fig. 3c)[26,27]. Consequently, the downward-shifted $L308^{7.56}$ one turn below $Y305^{7.53}$ plays an essential role as a structural pivot in the active conformation, as well as a member of the hydrophobic binding site for $L353^{H5.20}$ and $L358^{H5.25}$ of the C-terminal α5 helix of $G\alpha_q$, in addition to $M249^{6.36}$, $V246^{6.33}$, $L223^{5.65}$, $I134^{3.54}$, and $R130^{3.50}$ (Fig. 3d).

Ji et al. reported cryo-EM models of ET-1-bound ET_AR and ET_BR coupled to mini$G_{s/q}$, as well as a selective peptide IRL1620-bound ET_BR coupled to G_i, providing valuable structural insights into these complexes[31]. Their findings suggest that interface regions between ETRs and $G_{i/q}$ in the structures of ET_AR and ET_BR bound to ET-1 resemble the interface observed in our ET_BR–G_i complex structure. This implies that both ET-1-bound ET_AR and ET_BR engage G_i and G_q in a manner similar to the hydrophobic binding pocket of $L348^{H5.20}$, $L353^{H5.25}$, and $S373/S390^{8.47}$, interacting with the C-terminal end of the α5 helix. However, the deposited structures (PDB code 8HCQ, 8HCX, 8HBD) show some ambiguities. Discrepancies in the extracellular region, such as lack of disulfide bonds C158/C239 and C69/C341 in ET_AR, C174/C255 in ET_BR, and C3/C11 in ET-1–ET_BR, could affect structural interpretation. Furthermore, Sano et al. presented the cryo-EM structure of the ET-1–ET_B–G_i complex[33]. They observed a downward shift of the cytoplasmic side of TM7, consistent with our results. Although they used different constructs for G_i protein, including the linker between ET_BR and β subunit of G_i, their findings were consistent with the overall structure of the ET-1–ET_BR–DNG_{i1}–scFv16 complex. Notably, they described binding of the C-terminal α5 helix of $G\alpha_i$ to ET_BR as "shallow;" however, we have highlighted that the C-terminal wavy hook of $G\alpha_i$ is in a relatively deeper position than that in other G_i-coupled GPCRs, indicating a more vertical orientation in binding. The nearly identical structures with significant differences collectively contribute to a deeper understanding of the structural basis of ET_AR and ET_BR activation, their interactions with various G proteins, and the details of the ligand binding interface.

Materials and methods

Expression and purification of ET_BR

We used a previously described human ET_BR construct with cleavable N- and C-terminal tags. The N-terminus was modified to include the hemagglutinin signal peptide followed by a Flag tag. Rhinovirus 3C protease recognition site (LEVLFQGP) was introduced between G57 and L66. The C-terminus was truncated at S407; three cysteine residues were mutated to alanine (C396A, C400A, and C405A), as described[20]; and fused with an EGFP-HiS9 tag[22], following rhinovirus 3C protease recognition site. The $R124^{1.55}Y$ mutation was introduced to increase thermostability[21]. The resulting construct was introduced into the pFastBac vector. Recombinant baculovirus was prepared using the Bac-to-Bac baculovirus expression system (Invitrogen). *Spodoptera frugiperda* Sf9 insect cells (Invitrogen) were infected with the virus at a cell density of 3.0–4.0 ×10^6 cells/mL in Sf900 II medium and cultured for 48 h at 27 °C. To purify ET_BR, harvested cells were lysed with hypotonic lysis buffer (20 mM HEPES [pH 7.5], 0.1 μM ET-1, and protease inhibitors) and centrifuged at 30,000 ×*g* for 20 min. The pellet was homogenized with a Dounce homogenizer in a solubilization buffer (1% lauryl maltose neopentyl glycol (LMNG, Anatrace), 0.1% cholesteryl hemisuccinate (CHS, Sigma-Aldrich), 20 mM HEPES [pH 7.5], 200 mM NaCl, 20% glycerol, 0.2 μM ET-1, and protease inhibitors) and solubilized for 1 h at 4 °C. The insoluble cell debris was removed by centrifugation (30,000 ×*g*, 20 min), and the supernatant was

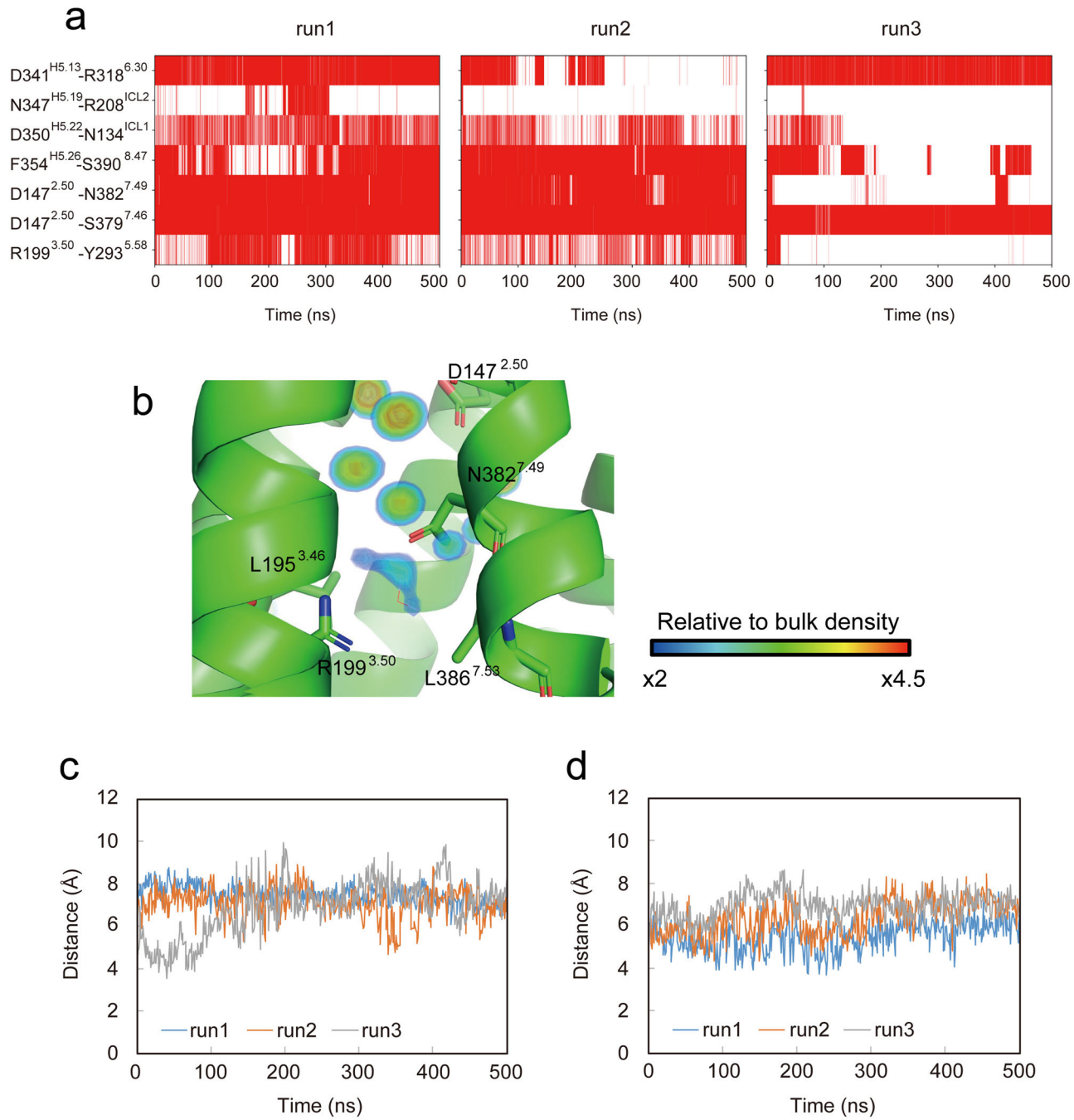

Fig. 6 | Intermolecular and intramolecular interactions observed in MD simulations. a Hydrogen-bond interactions in each run are represented by red lines. **b** Water densities in the cavity formed by transmembrane regions TM3, TM6, and TM7 in run 1 are superposed on the initial structure. Time evolution of distances between R199$^{3.50}$ and N382$^{7.49}$ (**c**) and between L195$^{3.46}$ and L386$^{7.53}$ (**d**) are shown. Distances were calculated as the minimum distance between all possible pairs of heavy atoms of two residues.

mixed with TALON cobalt resin (Clontech) for 2 h at 4 °C. The resin was collected in an open glass column, washed with 10 column volumes of wash buffer I (0.01% LMNG, 0.001% CHS, 20 mM HEPES [pH 7.5], 500 mM NaCl, 20% glycerol, and 10 mM imidazole), washed with 5 column volumes of wash buffer II (0.01% LMNG, 0.001% CHS, 20 mM HEPES [pH 7.5], 100 mM NaCl, 10% glycerol, and 10 mM imidazole), and eluted in wash buffer II supplemented with 250 mM imidazole. The eluate was concentrated, mixed with ET-1 to 1 μM, and dialyzed against a buffer containing 0.01% LMNG, 0.001% CHS, 20 mM HEPES (pH 7.5), 100 mM NaCl, 10% glycerol, 0.1 mM TECP, and His-tagged rhinovirus 3 C protease (made in-house) overnight at 4 °C. Following the cleavage of the N-terminus and EGFP–His10 by His-tagged 3 C protease, the sample was mixed with TALON resin for 1 h at 4 °C to remove cleaved EGFP–His10. The ET_BR-containing flow-through was concentrated and purified by size-exclusion chromatography on a Superdex 200 Increase 10/300 GL gel-filtration column (Cytiva) in a final buffer (100 mM NaCl, 20 mM HEPES [pH 7.5], 5% glycerol, 0.01% LMNG, 0.001% CHS and 0.1 μM ET1). Peak fractions were pooled and concentrated to 4–5 mg/mL.

Expression and purification of heterotrimeric wild-type G_{i1} and DNG_{i1}

Wild-type G_{i1} and DNG_{i1} heterotrimers were expressed in Sf9 or *Trichoplusia ni* Hi5 insect cells (Expression Systems) and purified as described[34].

In brief, insect cells were coinfected with two recombinant viruses: one encoding wild-type human $G\alpha_{i1}$ or $DNG\alpha_{i1}$ containing four mutations (S47N, G203A, E245A, A326A) and another encoding wild-type human $G\beta_1$ and $G\gamma_2$ subunits with a hexa-histidine tag inserted at the amino terminus of the $G\beta_1$ subunit. Cultures were collected 48 h after infection. Cells were lysed in hypotonic buffer, and lipid-modified heterotrimeric G_{i1} or DNG_{i1} was extracted in buffer containing 0.7% sodium cholate, 0.01% LMNG–0.001% CHS, 20 mM HEPES (pH 7.5), 100 mM NaCl, 5 mM $MgCl_2$, 1 mM TCEP, 50 μM GDP, and protease inhibitors. The soluble fraction was purified using TALON cobalt resin, and the detergent was exchanged from sodium cholate to 0.01% LMNG–0.001% CHS on a column. After elution was complete, the concentrated protein was dialyzed against a buffer containing 20 mM HEPES (pH 7.5), 100 mM NaCl, 1 mM $MgCl_2$, 0.1 mM TCEP, 10 μM GDP, 0.01% LMNG, 0.001% CHS, and His-tagged rhinovirus 3 C protease overnight at 4 °C to cleave the N-terminal His-tag. Then, the sample was mixed with TALON resin for 1 h at 4 °C to remove the cleaved His-tag. The flow-through fraction, containing wild-type G_{i1} or DNG_{i1} heterotrimers, was concentrated and purified by size-exclusion chromatography on a Superdex 200 Increase 10/300 GL gel-filtration column in a final buffer (20 mM HEPES [pH 7.5], 100 mM NaCl, 1 mM $MgCl_2$, 0.1 mM TCEP, 10 μM GDP, 0.01% LMNG and 0.001% CHS). Peak fractions were pooled and concentrated to approximately 20 mg/mL.

Expression and purification of scFv16

Single-chain Fab16 (scFv16) was expressed and purified as described[18,24]. In brief, scFv16 tagged with hexa-histidine at the C-terminus was expressed with a signal peptide in Hi5 insect cells using the Bac-to-Bac baculovirus expression system. The scFv16 secreted into the culture medium was purified by Ni-NTA (Qiagen) chromatography, following addition of Tris (pH 8.0) to the culture supernatant. The Ni-NTA eluent was dialyzed against a buffer consisting of 20 mM HEPES (pH 7.5), 100 mM NaCl, 0.1 mM TCEP, and rhinovirus 3 C protease overnight at 4 °C. The sample was mixed with TALON resin for 1 h at 4 °C to remove the cleaved His-tag. The flow-through fraction containing scFv16 was concentrated and purified by gel-filtration chromatography in a final buffer (100 mM NaCl and 20 mM HEPES [pH 7.5]). Peak fractions were pooled and concentrated to approximately 60 mg/mL.

Purification of the ET_BR–G_{i1}–scFv16 complex

The ET_BR–G_{i1}–scFv16 complex was prepared as described[18,28]. Purified ET_BR was mixed with a 1.2 molar excess of wild-type or dominant negative G_{i1} heterotrimer. The coupling reaction proceeded at 20–24 °C for 2 h, followed by incubation for 1 h at 4 °C with apyrase and λ-phosphatase (New England Biolabs) together with 1 mM $MnCl_2$ and 5 mM $MgCl_2$ for the hydrolysis of unbound GDP and dephosphorylation of proteins, respectively. Furthermore, 1.2 molar excess of scFv16 was added to the mixture and incubated for 2 h at 4 °C. The coupling mixture was incubated with 2A5 anti-ET_BR immunoaffinity resin overnight at 4 °C[35]. Complex-bound resin was first washed in a buffer containing 0.1% LMNG, 0.01% CHS, and 0.0003% glyco-diosgenin (GDN), then washed in gradually decreasing concentrations of LMNG and increasing concentrations of GDN. The complex was eluted in 20 mM HEPES (pH 7.5), 150 mM NaCl, 0.1 mM TCEP, 2 mM EDTA, 5% glycerol, 0.00375% LMNG, 0.000375% CHS, 0.00125% GDN, 0.1 μM ET-1, and 300 μg/mL 2A5 peptide (VPKGDRTAGSPPRTI) at room temperature. Finally, the ET_BR–G_{i1}–scFv16 complex was purified by size-exclusion chromatography on a Superdex 200 Increase 10/300 GL in 20 mM HEPES (pH 7.5), 100 mM NaCl, 0.1 mM TCEP, 0.1 μM ET-1, 0.00075% LMNG, 0.000075% CHS, and 0.00025% GDN. Peak fractions were concentrated to approximately 30 mg/mL for electron microscopy studies.

Collection of Cryo-EM Data

Proteins for cryo-EM were prepared to ~6 and 4 mg/mL for ET-1-bound ET_BR–wild-type G_{i1}–scFv16 (ET_BR–WTG_i) and ET-1-bound ET_BR–DNG_{i1}–scFv16 (ET_BR–DNG_i), respectively. Protein solution (3 μL) was applied to glow-discharged holey carbon grids (200 mesh Quantifoil R2/2 molybdenum and 200 mesh Quantifoil R1.2/1.3 copper for ET_BR–WTG_i and ET_BR–DNG_i, respectively), blotted, and plunged into liquid ethane at −182 °C using an EM GP2 plunger (Leica, Microsystems, Vienna, Austria) and Vitrobot Mark IV (Thermo Fisher Scientific) for ET_BR–WTG_i and ET_BR–DNG_i, respectively. Data were collected at OIST on a Talos Arctica (Thermo Fisher Scientific, Hillsboro, USA) electron microscope at 200 kV, equipped with a Falcon 3 camera (Thermo Fisher Scientific) and at SPring-8 on a CRYO-ARM300 electron microscope (JEOL) at 300 kV, equipped with a K3 camera (Gatan) (Supplementary Figs. 1, 2). An in-column energy filter with a slit width of 20 eV was inserted to acquire movie frames using CRYO-ARM300. Movies were recorded using EPU software (Thermo Fisher Scientific) on a Talos Arctica at a nominal magnification of 92,000× in counting mode and a pixel size of 1.094 Å at the specimen level, with a dose rate of 0.93 e- per physical pixel per second. Exposure time was 51.3 s, resulting in an accumulated dose of 40 e- per $Å^2$. Each movie included 40 fractioned frames. The movies were recorded using SerialEM[36] and JAFIS Tool version 1 (JEOL) on a CRYO-ARM300 at nominal magnifications of 60,000× and 100,000× in counting mode. The AI detection of each center hole position was performed using yoneoLocr, which prevented any stage alignment failures[37]. The pixel sizes at the specimen level were 0.816 and 0.507 Å for magnifications of 60,000× and 100,000×, with dose rates of 8.3 and 3.4 e- per physical pixel per second, resulting in an accumulated dose of ~76 and ~65 e- per $Å^2$ for 6.1 s and 4.9 s exposures, respectively. Each movie included 61 fractioned frames.

Image processing

All stacked frames were motion corrected with MotionCor2[38]. Defocus was estimated using CTFFIND4[39]. All the particles picked using crYOLO[40] were analyzed with RELION 3.1[41] and selected by 2D classification (Table 1, Supplementary Figs. 1, 2). The initial 3D model was generated in RELION, and the particles were divided into four classes by 3D classification, resulting in only one good class. The 3D auto-refinement produced a map, after contrast transfer function refinement, Bayesian polishing, masking, and postprocessing. Particle projections were subjected to subtraction of the detergent micelle density followed by 3D auto-refinement, yielding a final map with resolutions of 4.61, 3.21, and 3.62 Å for ET_BR–WTG_i, ET_BR–DNG_i, and ET_BR after focused 3D classification[42], respectively, according to the gold-standard Fourier shell correlation using a criterion of 0.143 (Supplementary Figs. 3–5 for ET_BR–WTG_i, ET_BR–DNG_i, and ET_BR, respectively)[36]. Local resolution maps were calculated using RELION.

Model building and refinement of the ET_BR–G_{i1} complex

The atomic models of ET-1 bound ET_BR (PDB ID: 5GLH) and G_i–scFv (PDB ID: 6OS9) were fitted to cryo-EM maps of ET_BR–WTG_i and ET_BR–DNG_i, respectively, using Chimera[43]. Atomic model building was performed using COOT[44]. The manually modified model was refined in real space on PHENIX[45], and the COOT/PHENIX refinement was iterated until the refinements converged. Finally, statistics calculated using MolProbity[46] were checked. Figures were drawn using the Pymol Molecular Graphic System (Schrödinger)[47], UCSF Chimera[43], and UCSF ChimeraX[48].

MD simulations

The intracellular loop between TM5 and TM6 (residues 302–311) of ET_BR and α-helical domain of $G\alpha_i$ (residues 56–181, 234–240), which are missing in the cryo-EM structure, were modeled using modeller 9.24[49]. The X-ray crystallographic structures of the D2 dopamine receptor–G_i complex (PDB ID: 6VMS) and rhodopsin–G_i complex (PDB ID: 6CMO) were used as templates for modeling the intracellular loop of ET_BR (Supplementary Fig. 12) and the α-helical domain of $G\alpha_i$, respectively. The structure of ET-1-bound ET_BR–G_i was embedded in a solvated 1-palmitoyl-2-oleoyl-*sn*-glycero-3-phosphocholine (POPC) bilayer using the CHARMM-GUI server[50]. The protein structure was protonated using the default settings of the CHARMM-GUI server. The system was composed of 453 POPC molecules, 64,293 water molecules, and 0.15 M K^+/Cl^- ions adjusted to neutralize the

net charge of the entire system (Supplementary Table 6). The CHARMM36m force field[51,52] was used for proteins, ions, and POPC molecules[53]. The TIP3P model[54] was used for water. Energy minimization and equilibration were performed using the CHARMM-GUI protocol with additional distance restraints between the hydrogen-bond donor and acceptor atoms found in the cryo-EM structure. The parameters for the distance restraints were $r_0 = 0$ nm, $r_1 = 0.3$ nm, $r_2 = 0.4$ nm, and $k = 4000$ kJ mol^{-1} nm^{-2}. Then, additional three-step equilibrations were performed with decreasing force constant. Simulations of 50-, 30-, and 20-ns were performed with $k = 4000$, 1000, and 200 kJ mol^{-1} nm^{-2}, respectively. After equilibrium simulations, a production run was performed in the constant-*NPT* ensemble for 500 ns. The temperature was maintained at 303.15 K using the Nose–Hoover thermostat[55,56] with a coupling constant of 1.0 ps. The pressure was maintained at 1.0 bar using a Parrinello–Rahman barostat[57] with a coupling constant of 5.0 ps. Electrostatic interactions were calculated using the particle mesh Ewald method[58] with a real space cutoff of 1.2 nm. Van der Waals interactions were calculated with a modified Lennard–Jones potential, where the force was smoothly switched to zero between 1.0 and 1.2 nm. The lengths of the bonds involving hydrogen atoms were constrained using the LINCS algorithm[59,60] to allow for the use of a time step of 2 fs. The simulations were repeated three times with different initial velocities. All simulations were performed using GROMACS 2022.4[61].

Probabilities of hydrogen-bond formation in the MD simulations were calculated using the "gmx hbond" tool with default settings. To calculate the density of water molecules, each snapshot of the trajectories was translated and rotated to superpose Cα atoms of ET_BR on the corresponding atoms of the initial structure. A cubic grid with a spacing of 0.4 Å was then created. Water density (ρ_i) at grid point i was calculated as follows:

$$\rho_i = \frac{1}{TV_r}\sum_{t=1}^{T}\sum_{j=1}^{N} H\left(r - \left|\mathbf{x}_{j,t} - \mathbf{c}_i\right|\right),$$

where T is the number of snapshots in the trajectories, N is the number of water molecules in the system, V_r is the volume of a sphere with radius r ($r = 1$ Å), $\mathbf{x}_{j,t}$ represents the coordinates of the oxygen atom of the j-th water molecule of the t-th snapshot, $\mathbf{c}_i$ is the coordinate of the grid point i, and $H(x)$ is the Heaviside step function.

NanoBiT G-protein dissociation assay

G_i activation was measured using a NanoBiT G-protein dissociation assay[7], in which heterotrimeric G-protein dissociation catalyzed by GPCR was monitored using a NanoBiT system (Promega). A large fragment (LgBiT) of NanoBiT luciferase was inserted into $G\alpha_{i1}$, and a small fragment (SmBiT) was N-terminally fused to a C68S-mutated $G\gamma_2$. The amino acid sequences of the NanoBiT G-protein constructs used in this study are identical to those in Inoue et al. [7]. The genes coding for the NanoBiT G-protein constructs, untagged $G\beta_1$ construct, and Flag-tagged ET_BR were synthesized and cloned into pCAG vectors (provided by Dr. Jun-ichi Miyazaki at Osaka University, Japan) or pcDNA3.1 expression plasmid by GenScript. Mixtures of plasmids prepared for transfection of HEK293A cells (Thermo Fisher Scientific) were prepared as described[7]. HEK293A cells were seeded in a 6-well culture plate at a concentration of 2 ×10^5 cells/mL (2 mL per well) one day before transfection. Transfection solution was prepared by combining 4 μL (per well hereafter) of polyethylenimine solution (Polysciences; 1 mg/mL) and a plasmid mixture consisting of 100 ng LgBiT-inserted Gα subunit ($G\alpha_{i1}$), 500 ng $G\beta_1$, 500 ng C68S-mutant SmBiT-fused $G\gamma_2$, and 200 ng wild-type or mutant ET_BR in 200 μL of Opti-MEM (Thermo Fisher Scientific). After 1-day incubation, transfected cells were collected with 0.5 mM EDTA-containing Dulbecco's PBS (D-PBS), centrifuged, and suspended in 2 mL of Hank's Balanced Salt Solution containing 0.01% bovine serum albumin (BSA; fatty-acid-free grade; SERVA) and 5 mM HEPES (pH 7.4) (assay buffer). The cell suspension was dispensed into a white 96-well plate (Greiner Bio-one) at a volume of 80 μL per well and loaded with 20 μL of 50 μM coelenterazine (Carbosynth) diluted in the assay buffer. After 2-h incubation at room temperature in the dark, baseline luminescence was measured (GloMax Navigator, Promega). A range of ET-1 solutions (20 μL of 0–6 × 10^{-6} M) were added and incubated for 3–5 min at room temperature before the second measurement. Luminescence counts were normalized to the initial count, and fold-change signals over vehicle treatment were used to evaluate the G-protein dissociation response. The G-protein activation signals were fitted to a 3-parametric concentration–response curve (GraphPad Prism 9.4), and pEC_{50} values and span values ("Top"–"Bottom") as E_{max} were obtained.

GloSensor cAMP assay

G_s activation was measured by the GloSensor cAMP accumulation assay, in which ET_BR-induced cAMP accumulation was assayed in cells transiently expressing a biosensor variant, with a cAMP binding domain fused to a luciferase mutant, according to the manufacturer's instructions (Promega). HEK293A cells were seeded in a 6-well culture plate at a density of 2.5 ×10^5 cells/mL (2 mL per well) one day before transfection. The cells were transfected with a mixture of pGloSensor cAMP 22 F plasmid (1.5 μg per well) and pCAG expression plasmid encoding ET_BR or mutant receptors (0.5 μg per well) using 6 μL of FuGENE HD transfection reagent (Promega) in 200 μL of Opti-MEM I reduced serum medium (Thermo Fisher Scientific). After 24 h of incubation, the transfected cells were harvested with 0.5 mM EDTA-containing D-PBS, centrifuged, and suspended in 2 mL of CO_2-independent medium containing 10% FBS (Invitrogen). The cell suspension was dispensed into a white 96-well plate at a volume of 80 μL per well and loaded with 20 μL of 5 mM D-luciferin in CO_2-independent medium containing 10% FBS. After 2 h incubation at room temperature in the dark, baseline luminescence was measured (GloMax Navigator, Promega). Varying concentrations of ET-1 solution (20 μL of 0–6 ×10^{-6} M) were added and incubated for 5 min at room temperature before the second measurement. Luminescence counts were normalized to the initial count. To evaluate the G_s-activated response, fold-change signals over vehicle treatment were represented as percentage of wild-type E_{max}. The activation signals were fitted to a three-parametric concentration–response curve (GraphPad Prism 9.4), and pEC_{50} and relative E_{max} values were obtained. Although a slight decrease was observed in the baseline without ET_BR expression plasmid (vehicle only) and increasing ET-1 concentration, we did not use phosphodiesterase inhibitors and pertussis toxins, because cAMP signals produced by ET_BR expression were sufficiently high in HEK293 cells (Supplementary Fig. 10e).

[^{125}I]ET-1 binding assay

In the NanoBiT G-protein dissociation assay and the cAMP accumulation assay, one quarter of the transfected cells were separately frozen in liquid nitrogen and stored at −80 °C. The numbers of wild-type or mutant ET_BRs expressed in the transfected cells were monitored by residual [^{125}I]ET-1 binding activity, reflecting correctly folded ET_BRs. A single-point binding assay using hydroxyapatite resin was performed as described[21]. Briefly, transfected cells were suspended in 50–100 μL of binding buffer containing 50 mM sodium phosphate buffer (pH 7.5), 2 mM $MgCl_2$, 0.1% BSA, and 0.1% digitonin. Then, 0.5–2 μL of samples (1.5–6 μg total protein) were incubated with approximately 150 pM [^{125}I]ET-1 (PerkinElmer) in 50 μL binding buffer at room temperature for 30 min. Hydroxyapatite resin (30 μL, BioRad) in 15% slurry was added to absorb receptor proteins, and the mixtures were centrifuged at 2000 rpm for 2 min to remove unbound [^{125}I]ET-1. Pelleted resin was washed with 0.3 mL of 50 mM sodium phosphate buffer (pH 7.5), 2 mM $MgCl_2$, and 0.1% digitonin and measured using a γ-counter. The count of [^{125}I]ET-1 bound in the presence of 100 nM ET-1 was subtracted as a background, which was approximately 10% or less of total binding. Each assay was performed in duplicate three times. Relative expression was represented as wild type 100%.

The apparent dissociation constants (K_d) of ET-1 for wild-type and mutant ET_B receptors expressed in HEK293A cell membrane were measured using saturation binding assays with [^{125}I]ET-1. The cell membranes containing ET_B receptors were incubated with eight different concentrations of [^{125}I]ET-1 ranging from 2.0 to 200 pM in 50 μl of 50 mM HEPES-NaOH, pH 7.5, 10 mM $MgCl_2$ (Mg-HEPES) buffer containing 0.1% BSA at

37 °C for 2 h. Binding reactions were terminated by dilution with cold Mg-HEPES, then were filtered onto glass fiber filters in 96-well plates (multi-screen HTS FB, Merck Millipore) pretreated with 0.1% BSA in Mg-HEPES, to separate the unbound [^{125}I]ET-1. After three washes with cold Mg-HEPES, the radioactivity captured by the filters was counted using a γ-counter. The non-specific binding of [^{125}I]ET-1 in each reaction was assessed by including 100 nM ET-1 in the same reaction. Assays were performed in duplicate three times and analyzed by fitting to a one-site binding equation (total and nonspecific) using GraphPad Prism 9.4.

Statistics and reproducibility

NanoBiT G-protein dissociation assay and GloSensor cAMP assay were analyzed using GraphPad Prism 9.4 (GraphPad) and are presented as mean ± standard error of the mean (SEM) from three to five independent experiments conducted in duplicate or triplicate. Statistical analyses were performed using Prism 9.4 (GraphPad) with one-way analysis of variance followed by Dunnett's multiple comparison of means test or Student's *t* test. Significance levels in statistical differences are indicated as (****$p < 0.0001$, ***$p < 0.001$, **$p < 0.01$, *$p < 0.05$ vs. WT).

Reporting summary

Further information on research design is available in the Nature Portfolio Reporting Summary linked to this article.

Data availability

The map and model generated in this study have been deposited in the EMDB and PDB with accession codes: EMD-38741 and PDB-8XWQ for the ET-1-bound ET_BR-wild-type G_{i1}-scFv16 complex, EMD-38740 and PDB-8XWP for the ET-1-bound ET_BR–DNG_{i1}-scFv16 complex and EMD-60404 and PDB-8ZRT for the focused 3D refinement of ET_BR in the ET-1-bound ET_BR–DNG_{i1}-scFv16 complex. All other study data including uncropped gel images are included in the article and/or Supplementary Data.

Received: 3 April 2024; Accepted: 16 September 2024;
Published online: 16 October 2024

References

1. Kedzierski, R. M. & Yanagisawa, M. Endothelin system: The double-edged swords in health and disease. *Annu. Rev. Pharmacol. Toxicol.* **41**, 851–876 (2001).
2. Davenport, A. P. et al. Endothelin. *Phamacol. Rev.* **68**, 357–418 (2016).
3. Barton, M. & Yanagisawa, M. Endothelin: 30 years from discovery to therapy. *Hypertension* **74**, 1232–1265 (2019).
4. Enevoldsen, F. C. et al. Endothelin receptor antagonists: status quo and future perspectives for targeted therapy. *J. Clin. Med.* **9**, 824 (2020).
5. Ranjan, A. K. & Gulati, A. Sovateltide mediated endothelin B receptors agonism and curbing neurological disorders. *Int. J. Mol. Sci.* **23**, 3146 (2022).
6. Doi, T., Sugimoto, H., Arimoto, I., Hiroaki, Y. & Fijiyoshi, Y. Interactions of endothelin receptor subtypes A and B with Gi, Go, and Gq in reconstituted phospholipid vesicles. *Biochemistry* **38**, 3090–3099 (1999).
7. Inoue, A. et al. Illuminating G-Protein-Coupling Selectivity of GPCRs. *Cell* **177**, 1933–1947 (2019).
8. Avet, C. et al. Effector membrane translocation biosensors reveal G protein and βarrestin coupling profiles of 100 therapeutically relevant GPCRs. *eLife* **11**, e74101 (2022).
9. Ballesteros, J. A. & Weinstein, H. Integrated methods for the construction of three dimensional models and computational probing of structure-function relations in G protein-coupled receptors. *Methods Neurosci.* **25**, 366–428 (1995).
10. Venkatakrishnan, J. et al. Diverse activation pathways in class A GPCRs converge near the G-protein-coupling region. *Nature* **536**, 484–487 (2016).
11. Weis, W. I. & Kobilka, B. K. The molecular basis of G protein-coupled receptor activation. *Annu. Rev. Biochem.* **87**, 897–919 (2018).
12. Thal, D. M., Glukhova, A., Sexton, P. M. & Christopoulos, A. Structural insights into G-protein-coupled receptor allostery. *Nature* **559**, 45–53 (2018).
13. Carpenter, B. & Tate, C. G. Active state structures of G protein-coupled receptors highlight the similarities and differences in the G protein and arrestin coupling interfaces. *Curr. Opin. Struct. Biol.* **45**, 124–132 (2017).
14. Manglik, A. & Kruse, A. C. Structural Basis for G Protein-Coupled Receptor Activation. *Biochemistry* **56**, 5628–5634 (2017).
15. Glukhova, A. et al. Rules of Engagement: GPCRs and G Proteins. *ACS Pharmacol. Transl. Sci.* **1**, 73–83 (2018).
16. Hilger, D. The role of structural dynamics in GPCR-mediated signaling. *FEBS J.* **288**, 2461–2489 (2021).
17. Venkatakrishnan, A. J. et al. Diverse GPCRs exhibit conserved water networks for stabilization and activation. *Proc. Natl Acad. Sci. USA* **116**, 3288–3293 (2019).
18. Koehl, A. et al. Structure of the μ-opioid receptor-G_i protein complex. *Nature* **558**, 547–552 (2018).
19. Mobbs, J. I. et al. Structures of the human cholecystokinin 1 (CCK1) receptor bound to Gs and Gq mimetic proteins provide insight into mechanisms of G protein selectivity. *PLoS Biol.* **19**, e3001295 (2021).
20. Shihoya, W. et al. Activation mechanism of endothelin ET_B receptor by endothelin-1. *Nature* **537**, 363–368 (2016).
21. Okuta, A., Tani, K., Nishimura, S., Fujiyoshi, Y. & Doi, T. Thermostabilization of the human endothelin type B receptor. *J. Mol. Biol.* **428**, 2265–2274 (2016).
22. Shihoya, W. et al. X-ray structures of endothelin ET_B receptor bound to clinical antagonist bosentan and its analog. *Nat. Struct. Mol. Boil.* **24**, 758–764 (2017).
23. Liang, Y.-L. et al. Dominant negative G proteins enhance formation and purification of agonist-GPCR-G Protein complexes for structure determination. *ACS Pharmacol. Transl. Sci.* **1**, 12–20 (2018).
24. Maeda, S. et al. Development of an antibody fragment that stabilizes GPCR/G protein complexes. *Nat. Commun.* **9**, 3712 (2018).
25. Doi, T., Kikuta, K. & Tani, K. Characterization of critical residues in the extracellular and transmembrane domains of the endothelin type-B receptor for propagation of the endothelin-1 signal. *Biochemistry* **59**, 1718–1727 (2020).
26. Thom, C. et al. Structures of neurokinin 1 receptor in complex with G_q and G_s proteins reveal substance P binding mode and unique activation features. *Sci. Adv.* **7**, eabk2872 (2021).
27. Harris, J. A. et al. Selective G protein signaling driven by substance P–neurokinin receptor dynamics. *Nat. Chem. Biol.* **18**, 109–115 (2022).
28. Kato, H. E. et al. Conformational transitions of a neurotensin receptor 1-G_{i1} complex. *Nature* **572**, 80–85 (2019).
29. Flock, T. et al. Universal allosteric mechanism for Gα activation by GPCRs. *Nature* **524**, 173–179 (2015).
30. Sun, D. et al. Probing $Gα_{i1}$ protein activation at single-amino acid resolution. *Nat. Struct. Mol. Biol.* **22**, 686–694 (2015).
31. Ji, Y. et al. Structural basis of peptide recognition and activation of endothelin receptors. *Nat. Commun.* **14**, 1268 (2023).
32. Peng, S. et al. Structures of human gastrin-releasing peptide receptors bound to antagonist and agonist for cancer and itch therapy. *Proc. Natl Acad. Sci. USA* **1ss20**, e2216230120 (2023).
33. Sano, F. K., Akasaka, H., Shihoya, W. & Nureki, O. Cryo-EM structure of the endothelin-1-ET_B-G_i complex. *eLife* **12**, e85821 (2023).
34. Dror, R. O. et al. Structural basis for nucleotide exchange in heterotrimeric G proteins. *Science* **348**, 1361–1365 (2015).
35. Yamaguchi, T., Arimoto-Tahara, I., Fujiyoshi, Y. & Doi, T. Characterization and application of monoclonal antibodies against human endothelin B receptor expressed in insect cells. *Biotech. Lett.* **26**, 293–299 (2004).
36. Rosenthal, P. B. & Henderson, R. Optimal determination of particle orientation, absolute hand, and contrast loss in single-particle electron cryomicroscopy. *J. Mol. Biol.* **333**, 721–745 (2003).

37. Yonekura, K., Maki-Yonekura, S., Naitow, H., Hamaguchi, Y. & Takaba, K. Machine learning-based real-time object locator/evaluator for cryo-EM data collection. *Commun. Biol.* **4**, 1044 (2021).
38. Zheng, S. Q. et al. MotionCor2: anisotropic correction of beam-induced motion for improved cryo-electron microscopy. *Nat. Methods* **14**, 331–332 (2017).
39. Rohou, A. & Grigorieff, N. Fast and accurate defocus estimation from electron micrographs. *J. Struct. Biol.* **192**, 216–221 (2015).
40. Wagner, T. & Raunser, S. The evolution of SPHIRE-crYOLO particle picking and its application in automated cryo-EM processing workflows. *Commun. Biol.* **3**, 61 (2020).
41. Zivanov, J. et al. New tools for automated high-resolution cryo-EM structure determination in RELION-3. *eLife* **7**, e42166 (2018).
42. Bai, X. C., Rajendra, E., Yang, G., Shi, Y. & Scheer, S. H. Sampling the conformational space of the catalytic subunit of human gamma-secretase. *eLife* **4**, e11182 (2015).
43. Pettersen, E. F. et al. UCSF Chimera-a visualization system for exploratory research and analysis. *J. Comput. Chem.* **25**, 1605–1612 (2004).
44. Emsley, P., Lohkamp, B., Scott, W. G. & Cowtan, K. Features and development of Coot. *Acta Cryst.* **D66**, 486–501 (2010).
45. Adams, P. D. et al. PHENIX: a comprehensive Python-based system for macromolecular structure solution. *Acta Cryst.* **D66**, 213–221 (2010).
46. Chen, V. B. et al. MolProbity: all-atom structure validation for macromolecular crystallography. *Acta Crystallogr. D. Biol. Crystallogr.* **66**, 12–21 (2010).
47. DeLano, W. L. *The PyMOL molecular graphics system* (DeLano Scientific, LCC, 2004).
48. Pettersen, E. F. et al. UCSF ChimeraX: Structure visualization for researchers, editors, and developers. *Protein Sci.* **30**, 70–82 (2021).
49. Martí-Renom, M. A. et al. Comparative protein structure modeling of genes and genomes. *Annu. Rev. Biophys. Biomol. Struct.* **29**, 291–325 (2000).
50. Jo, S., Kim, T., Iyer, V. G. & Im, W. CHARMM-GUI: A web-based graphical user interface for CHARMM. *J. Comput. Chem.* **29**, 1859–1865 (2008).
51. Huang, J. & MacKerell, A. D. CHARMM36 all-atom additive protein force field: Validation based on comparison to NMR data. *J. Comput. Chem.* **34**, 2135–2145 (2013).
52. Huang, J. et al. CHARMM36m: An improved force field for folded and intrinsically disordered proteins. *Nat. Methods* **14**, 71–73 (2016).
53. Klauda, J. B. et al. Update of the CHARMM all-atom additive force field for lipids: validation on six lipid types. *J. Phys. Chem. B* **114**, 7830–7843 (2010).
54. Jorgensen, W. L., Chandrasekhar, J., Madura, J. D., Impey, R. W. & Klein, M. L. Comparison of simple potential functions for simulating liquid water. *J. Chem. Phys.* **79**, 926–935 (1983).
55. Hoover, W. G. Canonical dynamics: Equilibrium phase-space distributions. *Phys. Rev. A* **31**, 1695–1697 (1985).
56. Nosé, S. A molecular dynamics method for simulations in the canonical ensemble. *Mol. Phys.* **52**, 255–268 (1984).
57. Parrinello, M. & Rahman, A. Crystal Structure and Pair Potentials: A Molecular-Dynamics Study. *Phys. Rev. Lett.* **45**, 1196–1199 (1980).
58. Darden, T., York, D. & Pedersen, L. Particle mesh Ewald: An *N*·log(*N*) method for Ewald sums in large systems. *J. Chem. Phys.* **98**, 10089–10092 (1993).
59. Hess, B., Bekker, H., Berendsen, H. J. C. & Fraaije, J. G. E. M. LINCS: A linear constraint solver for molecular simulations. *J. Comput. Chem.* **18**, 1463–1472 (1997).
60. Hess, B. P-LINCS: A parallel linear constraint solver for molecular simulation. *J. Chem. Theory Comput.* **4**, 116–122 (2008).
61. Abraham, M. J. et al. Gromacs: High performance molecular simulations through multi-level parallelism from laptops to supercomputers. *SoftwareX* **1**, 19–25 (2015).

Acknowledgements

This research was partially supported by the Platform Project for Supporting Drug Discovery and Life Science Research (Basis for Supporting Innovative Drug Discovery and Life Science Research) from AMED under Grant Numbers JP21am0101118, JP21am0101116, JP22ama121006, JP23ama121004, and JP23ama121027, JST-Mirai Program Grant Number JPMJMI23G2. R.K., M.H., and B.M.H. acknowledge the generous support of the Okinawa Institute of Science and Technology (OIST), Scientific Computing & Data Analysis Section, and Scientific Imaging Section at OIST and the Japanese Cabinet Office. R.K. acknowledges the support of Prof. Tsumoru Shintake. This work was supported by JSPS KAKENHI Grant Number 20H03210 (T.D.), ISHIZUE 2019 from the Kyoto University Research Development Program, and Center for Quantum and Information Life Sciences, University of Tsukuba. T.D. acknowledges the generous support of the laboratory members of Prof. Tochio at Kyoto University.

Author contributions

K.T. and T.D. designed the research, K.T., S.M.-Y, R.K., T.H., and T.D. performed the research, K.T., M.H., A.M., B.M.H., K.Y., and T.D. analyzed the data, T.N, and T.T. performed MD simulation, K.T., T.N., T.T., and T.D. wrote the manuscript, and all authors made editorial contribution.

Competing interests

The authors declare no competing interests.

Additional information

Supplementary information The online version contains supplementary material available at https://doi.org/10.1038/s42003-024-06905-z.

Correspondence and requests for materials should be addressed to Kazutoshi Tani or Tomoko Doi.

Peer review information *Communications biology* thanks Jagannath Maharana, Sadashiva Karnik and the other, anonymous, reviewer(s) for their contribution to the peer review of this work. Primary Handling Editors: Janesh Kumar and Laura Rodríguez Pérez. A peer review file is available.